Article type : Original Manuscript

Morphodynamics and depositional signature of low-aggradation cyclic steps: New insights from a depth-resolved numerical model

Age J. Vellinga (1,2) , Matthieu J.B. Cartigny (2,3) , Joris T. Eggenhuisen (4), Ernst W.M. Hansen (5)

(1) School of Ocean and Earth Science, University of Southampton, National Oceanography Centre European way, Southampton, UK SO14 3ZH (a.j.vellinga@soton.ac.uk)
(2) National Oceanography Centre, University of Southampton Waterfront Campus, European Way, Southampton, UK SO14 3ZH
(3) Departments of Earth Sciences and Geography, Durham University, South Road, Durham, UK DH1 3LE
(4) Department of Earth Sciences, Utrecht University, Heidelberglaan 2, 3584 CS, Utrecht, The Netherlands
(5) Complex Flow Design A.S., Havnegata 9, 7010, Trondheim, Norway

Abstract (A)

Bedforms related to Froude-supercritical flow, such as cyclic steps, are increasingly frequently observed in contemporary fluvial and marine sedimentary systems. However, the number of observations of sedimentary structures formed by supercritical flow bedforms remains limited. The low number of observations might be caused by poor constrains on criteria to recognise these associated deposits. This study provides a detailed quantification on the mechanics of a fluvial cyclic step system, and their depositional signature. A computational fluid-dynamics model is employed to acquire a depth-resolved image of a cyclic step system. New insights into the mechanics of cyclic steps shows that: (i) the hydraulic jump is, in itself, erosional; (ii) there are periods over which the flow is supercritical throughout and there is no hydraulic jump, which plays a significant role in the morphodynamic behaviour of cyclic steps; and (iii) that the depositional signature of cyclic steps varies with rate of aggradation. Previous work has shown that strongly aggradational cyclic steps, where most of the deposited sediment is not reworked, create packages of backsets, bound upstream and downstream by erosive surfaces. Here the modelling work is focussed on less aggradational conditions and more transportational systems. The depositional signature in such systems is dominated by an amalgamation of concave-up erosional surfaces and low-angle foresets and backsets creating lenticular bodies. The difference between highly aggradational cyclic steps and

This is an Accepted Article that has been peer-reviewed and approved for publication in the Sedimentology, but has yet to undergo copy-editing and proof correction. Please cite this article as an “Accepted Article”; doi: 10.1111/sed.12391

low aggradation steps can be visible in outcrop both by the amount of erosional surfaces, as well as the ratio of foreset to backset, with backsets being indicative of more aggradation.

Keywords: Aggradation, backset, bedform, cyclic steps, Froude, scour, supercritical

Introduction (A)

Large quantities of sediment are transported by high-discharge events, such as floods or jökulhlaup (Nordin and Beverage, 1965). Such events are prone to Froude-supercritical flow, where surface waves cannot migrate upstream because the flow velocity exceeds the wave-propagation velocity. Froude-supercritical unidirectional sediment-laden flow over an erodible sediment bed leads to the formation of bedforms, such as antidunes (Kennedy, 1969; Alexander et al., 2001), and at higher Froude numbers cyclic steps (Winterwerp et al., 1992; Parker, 1996; Taki and Parker, 2005; Kostic et al., 2010; Cartigny et al., 2014). Transitional bedforms, such as unstable antidunes and 'chutes and pools', populate the bedform stability diagram at flow-intensities between antidunes and cyclic steps (Alexander et al., 2001; Cartigny et al., 2014; Kostic, 2014). Supercritical flow conditions in fluvial settings (which are open-channel flows) creating supercritical-flow bedforms, have been reported in mountain streams (Kostic et al., 2010), on glacial outwash planes (Lang and Winsemann, 2013) and on beaches and dredging disposal sites (Winterwerp et al., 1992). Froude-supercritical conditions are reached more quickly in sediment gravity flows, such as turbidity currents and pyroclastic flows, due to the small density contrast between the flow and the ambient fluid that reduces the wave-propagation velocity. The large number of observations of Froude-supercritical flow related bedforms on the sea floor, mainly found in submarine canyons and steep delta slopes, reaffirms the prevalence of Froude-supercritical flows in marine settings (Symons et al., 2016).

Developments in physical and numerical modelling of supercritical-flow bedforms (Kennedy, 1969; Jorritsma, 1973; Foley, 1977; Winterwerp et al., 1992; Parker and Izumi, 2000; Alexander et al., 2001; Fagherazzi and Sun, 2003; Sun and Parker, 2005; Taki and Parker, 2005; Fildani et al., 2006; Kostic and Parker, 2006; Alexander, 2008; Sequeiros et al., 2009; Spinewine et al., 2009; Kostic et al., 2010 Paull et al., 2010; Cartigny et al., 2011; Kostic, 2011; Balmforth and Vakil, 2012; Cartigny et al., 2014) have sparked a large number of observations of supercritical-flow bedforms in modern systems (Fildani et al., 2006; Lamb et al., 2008; Duarte et al., 2010; Jobe et al., 2011; Hughes Clarke et al., 2012; Babonneau et al., 2013; Maier et al., 2013; Covault et al., 2014; Fricke et al., 2015;

Tubau et al., 2015; Zhong et al., 2015; Normandeau et al., 2016; Symons et al., 2016). Despite this common and well-documented occurrence of supercritical-flow bedforms, outcrop examples of deposits indicating these flow-conditions in a fluvial setting (Fielding, 2006; Duller et al., 2008; Fielding et al., 2009; Ghienne et al., 2010; Lang and Winsemann, 2013) or in a (deltaic-) marine setting (Postma et al., 2009; Postma et al., 2014; Ventra et al., 2015; Dietrich et al., 2016) are sparse. The recent flurry of recognition of supercritical bedforms in modern environments makes it implausible that sedimentary structures indicative of these bedforms should be rare in deposits formed in comparable ancient environments.

The sparsity of supercritical sedimentary structures is often attributed to poor preservation potential of supercritical-flow-regime deposits, due to reworking by subcritical flows in the waning stages of high-discharge events. Froude-supercritical flows also tend to form in parts of the sedimentary system that are net-erosive on a geological timescales, such as mountainous terrains (Middleton, 1965; Foley, 1977; Yagishita and Taira, 1989; Wynn and Stow, 2002; Fielding, 2006; Duller et al., 2008; Ponce and Carmona, 2011; Lang and Winsemann, 2013; Macdonald et al., 2013; Cartigny et al., 2014; Postma et al., 2014; Ventra et al., 2015). An alternative explanation for the sparse recognition of supercritical regime facies is that their depositional signature is poorly understood.

Transportational cyclic steps in open-channel flows, which are neither net-erosive nor net-depositional (Parker and Izumi, 2000), have been modelled experimentally in flume tanks (Taki and Parker, 2005; Cartigny et al., 2014) and modelled numerically using depth-averaged models (Fagherazzi and Sun, 2003). Cyclic steps in subaqueous settings have been modelled in flume experiments (Spinewine et al. 2009) and with depth-averaging numerical models (Fildani et al., 2006; Kostic and Parker, 2006; Kostic et al., 2010; Cartigny et al., 2011; Kostic, 2011; Covault et al., 2014; Kostic, 2014; Covault et al., 2016). These studies have provided valuable insight into the development and mechanics of cyclic steps, by exploring how average flow velocity, sediment concentration and flow thickness vary over the length of the bedform wavelength (Fig. 1). These depth-averaged studies have also shown how the co-variation of these three average properties leads to upstream migrating cyclic steps, caused by erosion beneath the accelerating supercritical flow over the lee-side, and deposition beneath the subcritical flow over the stoss-side. The transition between the supercritical flow regime and the subcritical flow regime is characterised by a hydraulic jump, where the flow abruptly expands and decelerates. Little is known about the vertical variation in flow velocity, sediment concentration, and turbulence, that occur over a cyclic step bedform, because this variation is hard to constrain with experimental measurements and averaged out in depth-averaged modelling studies. These parameters are, however, crucial to linking flow dynamics to the sedimentary architecture and facies variation over time and space. Moreover, interpreting supercritical-flow processes from outcrops and cores is strongly dependent on distinguishing small scale facies characteristics.

The aim of this study is two-fold: (i) quantifying flow properties in a depth-resolved manner to understand the mechanics of a fluvial cyclic step system; and (ii) linking the flow dynamics of a cyclic step system to the depositional signature to predict what type of deposits are expected to be associated with cyclic steps.

Methods (A)

Linking large-scale bedforms and associated facies to flow dynamics in a numerical model is possible if the depositional and erosive processes are fully resolved. Ideally such model would include a three-dimensional distribution of all fluid and grain velocities, sediment concentrations and grain sizes. Such a model would also take into account intergranular interactions between individual grains and have a two-way coupling, in which sediment is affected by fluid motion and vice-versa. Direct Numerical Simulations (DNS) are now capable of resolving all of these processes to the individual grain scale (e.g. Cantero et al., 2008; Soldati and Marchioli, 2012; Kidanemariam and Uhlmann, 2014). However, DNS is presently only viable for a small number of grains, in a relatively small spatial domain, and at low Reynolds numbers, due to the high computational power required for DNS. Because of the computational limitation on DNS, it is not a feasible method to model cyclic steps in natural flows, which have high Reynolds numbers, a large number of grains and are to be simulated over a longer timescale.

Reynolds-Averaging Navier-Stokes (RANS) models, like DNS models, employ the Navier-Stokes equations: the mass-conservation and momentum-conservation equations that describe the motion of fluids (Eqs 1.1 to 1.4 in the Appendix). Unlike DNS, RANS models do not solve the Navier-Stokes equations to the smallest spatial and temporal scale at which eddies can occur, the Kolmogrov scale, but solve time-averaged equations and use a turbulence model to approximate the small-scale turbulence. By using a RANS-approach, the computational time can be greatly reduced. Vertical variation is however maintained, in contrast to previous depth-averaging models. In this study the RANS model FLOW-3D® (FlowScience, Santa Fe, New Mexico) is used, in combination with a two-equation k-ε renormalisation group (RNG) turbulence model, applying the turbulent viscosity assumption, for details see Appendix I. Basani et al. (2014) and Ge et al. (2017) use the same model to simulate turbidity currents and can provide further detail.

Sediment transport models (B)

Individual sediment transport models are used to compute bed-load transport and suspended-load transport. Grain–grain interactions are not incorporated into the suspension model, something which starts to play a significant role at sediment concentrations >9 vol.% (Bagnold, 1954). Neither does the model take into account any turbulence modification as a result of suspended sediment.

The onset of sediment movement depends on the shear stress exerted on the bed, which mobilises the sediment, and the submerged weight of the grains, resisting mobilisation. The bed shear stress is non-dimensionalised in the Shields parameter (θ), using sediment particle scales and fluid scales (Eq.2.1 in the Appendix). Sediment is transported if the local Shields parameter exceeds the critical shields parameter (θ_{cr}). The critical Shields parameter is described by the Shields-curve, which is approximated by an algebraic expression as formulated in Guo (2002; Eq. 2.2). The critical Shields parameter is corrected for slope effects (Eq. 2.4) as slopes in cyclic step systems can reach up to 15 degrees.

Bed-load transport (C)

Bed-load transport consists of the saltation and rolling of sediment along the bed, and is modelled using the empirical equation (Eq. 2.5) of Meyer-Peter and Müller (1948). The scalar quantity of bed-load transport is converted into a bed-load velocity vector, which is required to compute a directional bed-load flux (Eq. 2.6). This is done by using the bed-load thickness (Eq. 2.7), as approximated by Van Rijn (1984), and by assuming that the direction of transport is the same as the flow direction of the fluid cell closest to the bed.

Suspended-load transport (C)

Three aspects of suspended load transport are simulated: (i) sediment entrainment into suspension; (ii) sediment settling out of suspension – these two opposing processes occur simultaneously; and (iii) advection and turbulent diffusion of sediment.

A sediment-entrainment flux is expressed as a lift velocity (Eq. 2.8), which is the flux divided by the computational cell area (Mastbergen and Van Den Berg, 2003). Similarly, the settling mass-flux of sediment is calculated using Eq. 2.9 (Soulsby, 1997). The sediment velocity is calculated using the settling velocity and bulk flow velocity (Eq. 2.10). The suspended sediment concentration at a given location is computed by solving a transport equation (Eq. 2.11). The transport equation for suspended sediment incorporates both advection, using the sediment velocity from Eq. 2.10 and diffusion through turbulence.

Simulation setup (B)

To validate the model, the simulations are compared to an experimental study on fluvial cyclic steps (Cartigny et al., 2014). Their flume setup in the EUROTANK flume laboratory is here reproduced numerically. The focus is on two experimental runs (9 and 15) which produced a stable train of cyclic steps.

The experimental flume is modelled using a meshed volume (Fig. 2) of 12.0 m by 0.15 m by 1.0 m, in the x, y and z-directions (Table 1). The width in the flow-normal y-direction has been downsized to save computational time. Boundary conditions consist of: an inflow condition, with a specified discharge, at the x = 0 m, an outflow at x = 12 m, a no-slip wall condition on the Y_{min} and Y_{max} boundaries, the sides of the flume tank, and a wall on the Z_{min} boundary, the flume tank bottom.

A smooth sediment bed of 350 µm diameter grains (medium sand) was placed on the bottom of the modelled flume tank with a slope of 0.5 degrees. Near the outflow boundary a non-erodible wedge is introduced to mimic a standing body of water located at the flume expansion tank, which prevents excessive erosion. The initially smooth sediment bed interacts dynamically to the flow conditions by erosion and deposition.

Numerical simulation 1 reproduced run 9 performed in the laboratory, with a specific discharge of 0.077 m^2/s and grain size of 350 µm. Simulation 2 reproduced run 15, with a specific discharge of 0.093 m^2/s, and grain size of 350 µm (see Table 2 for details).

Validation of the model (B)

The evolution of bed and water surface elevations display qualitative and quantitative agreement between physical and numerical simulation (Table 3 and Fig. 3). A series of cyclic steps formed spontaneously from the initially smooth bed. Erosion and deposition in the model is validated by comparing the rates at which the cyclic steps migrate. The period of bedform migration is 109 seconds in the numerical model (numerical simulation 1), and 85 seconds in the experimental results. Cartigny et al. (2014) suggest that the period of migration of cyclic steps in the simulations was generally between 80 and 120 seconds, a range consistent with the numerical results.

Because flow over a cyclic step is variable by nature, a comparison is made between both the median and 90th percentile of the Froude number from the Froude number time-series. Froude numbers of the numerical simulations appear to be in close correspondence to the experimental models (Fig. 3), the Froude numbers are generally <10% higher; there is however a 21% increase in median Froude number in simulation 1. Based on the similarity in migration period and Froude number variation the numerical model is assumed to give a valid representation of the cyclic step process.

Flow characteristics (A)

The interactions between the flow dynamics and the bedforms morphology in simulation 2 are here described in detail. The focus is on simulation 2, because the data in Table 3 show that simulation 2 is the closest match to the physical observations. Supplementary video 1 shows the flow character and the interaction with the bed, and visually complements the sections on *Flow characteristics* and *Morphodynamics*.

General character (B)

Observation (C)

The simulated flow creates cyclic steps that are typically 1.5 to 2.0 m in wavelength and 10 to 15 cm in amplitude, and are associated with flows of 5 to 15 cm thick (for example, Fig. 4). The flow character shows that a hydraulic jump is located in or around the trough of the bedform, separating a supercritical flow on the lee side of the bedform from a subcritical flow over the stoss side (Fig. 4). In the simulations it is observed that the hydraulic jump is present 89% of the time, which is here referred to as state 1. Flow is supercritical from crest to crest during the remaining 11% of the time (state 2). When present, the hydraulic jump is located upstream of the trough centre 50% of the time, at the trough centre 35% of the time, and downstream of the trough centre 15% of the time. The hydraulic jump is associated with coherent flow structures, such as stationary eddies, rollers, where the water 'rolls' around and changes direction (Fig. 1). These rollers are associated with the hydraulic jump, and typically (80% of the time) located in the upper half of the flow. The remaining 20% of the time a roller forms in the lower half of the flow. The area in which rollers form is <50 cm long, starting at the initiation of the hydraulic jump, with the rollers themselves being 10 to 20 cm long and less than 10 cm high. A transition from subcritical flow to supercritical flow is present close the crest of the bedform on the stoss side of the cyclic step. The average Froude number at the crest of the bedform in the simulation was 1.22 (±0.15), based on an analysis of 29 individual cyclic steps.

Interpretation (C)

The character of the flow over a cyclic step generally corresponds with that of conceptual models based on laboratory experiments and field observations (Fig. 1; Winterwerp et al., 1992; Parker, 1996; Taki and Parker, 2005; Cartigny et al., 2014). The transition from the subcritical flow regime to supercritical flow regime, at a Froude-number of unity, is commonly presumed to be at the crest of a cyclic step (Winterwerp et al., 1992; Parker, 1996; Taki and Parker, 2005; Cartigny et al., 2014). The observations in simulations herein are however more in line with classical hydraulic work which shows that the Froude number at the crest of a curvilinear convex feature is expected to occur at Fr = 1.19 (Rouse, 1936).

Velocity field (B)

Observation (C)

The flow accelerates over the bedform from just after the hydraulic jump up to the next hydraulic jump. In the supercritical part of the velocities of 2 m/s are reached on the lee side of the bedform, and the velocity maximum is located near the free-surface. Within the region of the hydraulic jump a specific flow pattern develops; a high velocity layer located near the bed and a roller, associated with negative downstream flow velocities, is located on top of this layer (Fig. 4A and Fig. 5B1). In the subcritical part of the flow the flow velocities on the stoss side range from 0.5 to 1.0 m/s.

Interpretation (C)

The supercritical flow over the lee side of the bedform has a convex-downstream velocity profile with a large velocity gradient, creating significant shear on the sediment bed (Figs 5B4 and 5B5). In the region of the hydraulic jump the velocity profile is convex-downstream at the lowest section of the flow, and curved convex-upstream at the top section of the flow (Fig. 5B1), this flow structure is related to the rollers that develop in the hydraulic jump. The velocity profile downstream of the hydraulic jump (Figs 5B2 and Fig. 5B3) is not typical for open-channel flow as it inherits the unusual velocity profile caused by the hydraulic jump.

Sediment concentration (B)

Observation (C)

The average sediment concentration in the flow is 5.6% by volume. A clear increase in sediment concentration over the supercritical lee side of the cyclic steps is not observed (Figs 4B and 5C). At the region of the hydraulic jump, there is a clear difference in sediment concentration between the fast-flowing near bed layer, with concentrations between 5% and 10%, and the upper part of the flow, where sediment concentrations within the roller are less than 1% (Fig. 5C1 and 5C2). In the subcritical part of the flow the near-bed sediment concentrations range from 5 to 10% by volume. Sediment concentrations decrease towards the free surface, where they reach near-zero values (Fig. 4B).

Interpretation (C)

The lack of increase in sediment concentration over the lee side of the cyclic steps is counterintuitive, as one might think that entrainment of sediment into the flow increases the sediment concentration. However, the sediment discharge is the product of the sediment concentration and flow velocity. And while depth-average sediment concentration only increases from 7 to 9%, the sediment discharge doubles over the lee side (Fig. 6F). This doubling shows that an increasing velocity forms the dominant control on the sediment discharge and explains the counterintuitive sediment concentration trend. There is in an increase in stratification in the subcritical part of the flow, the sediment settles, causing higher sediment concentrations near the bed (Fig. 4B and Fig. 5C2 and 5C3).

Turbulence (B)

Observation (C)

Turbulent kinetic energy (TKE), the mean kinetic energy per unit-mass associated with turbulent eddies, is of the order of 0.01 to 0.03 J/kg in the supercritical part of the flow, with peak values near the bed where shear is highest (Fig. 5D4 and 5D5). These TKE levels are equivalent to 8 to 14 cm/s of turbulent velocity fluctuations assuming isotropic turbulence. TKE is three to ten times higher (0.1 J/kg) in the region of the hydraulic jump (Fig. 4C and Fig. 5D1). The subcritical region has the lowest turbulent kinetic energy, generally less than 0.01 J/kg.

Interpretation (C)

Turbulence is generated in flow regions where shear within the flow is high (i.e. the velocity gradient), such is the case at a hydraulic jump. Turbulence is the mechanism through which sediment is suspended and dispersed in the flow. Hence, in regions of high turbulence sediment is not prone to settle, despite having relatively high sediment concentrations. The combination of high turbulent energy, inhibiting settling, and a relatively high shear on the bed at the hydraulic jump is a likely cause for entrainment to outpace settling, causing the hydraulic jump region itself to be erosive.

Morphodynamics (A)

Relating the flow dynamics to bed surface evolution is crucial to understand how cyclic steps maintain their morphodynamic equilibrium. Described here are two states observed in a cyclic step system between which the system alternates (Fig. 7). *State 1* (89% of the time): there is a hydraulic jump present in the trough of the bedform, the flow is supercritical at the lee side of the cyclic step, and subcritical at the stoss side of the cyclic step. *State 2* (11% of the time): the flow is supercritical over the whole bedform and a hydraulic jump is absent, the flow over the stoss side of the bedform decelerates and thickens, but not enough to form a hydraulic jump. In state 2 the flow is still erosive over the lee side of the bedform, and depositional over the stoss side. The topographic difference between the trough of the bedform and the crest is lower in state 2 than in state 1. Supplementary videos 1 and 2 help to visualise and understand of the morphodynamics more clearly.

Flow state 1 (B)

Observation (C)

Supercritical flow is limited to the crest and lee side of the cyclic step in flow state 1. The excess shear stress, the shear stress that exceeds critical shear stress for movement on the bed (here 0.25 Pa), increases from 5 Pa at the crest of the bedform, to 13 Pa just before the hydraulic jump (Fig. 6C). An excess shear stress larger than 0 does not mean there is overall erosion, but simply that there is some sediment entrainment. It is the local balance between the sediment entrainment flux, which increases with shear stress, and the settling flux, which determines whether there is net erosion or net deposition.

The start of the hydraulic jump is typically located at the downstream end of the lee side and is associated with the transition from the lee side to the stoss side. The hydraulic jump is mildly erosive, illustrated by its location on the lee side (Fig. 6A). The excess shear stress decreases gradually from about 13 Pa to 5 Pa within the region of a hydraulic jump (Figs 6C and 4D).

After the flow has decelerated at the hydraulic jump, the flow slowly thins and accelerates again, while depositing sediment at the stoss side. The shear stress in the subcritical part of the flow is 4 to 5 Pa (Fig. 6C). Both the increase in bed-height and the decrease in sediment discharge (Fig. 6A and F) illustrate that the Froude-subcritical region is depositional.

In state 1, more sediment is deposited nearer the trough of the bedform than at its crest, causing the topography to decrease (Fig. 7D and E). As the topography decreases, the hydraulic jump is washed out and disappears.

Interpretation (C)

In state 1 the continuous acceleration of the supercritical flow over the lee side of the bedform leads to increased bed shear stress. Upstream of the crest of the bedform (0.95 to 1.0 on Fig. 6), shear stresses on the bed are low enough to allow the settling of sediment to outpace entrainment of sediment. Downstream of the crest of the bedform shear stress continuously increases, resulting in the sediment-entrainment flux to exceed the settling flux, making the flow erosive, as indicated by an increase in sediment discharge (Fig. 6F). The morphological effect of the supercritical flow is a curve at the crest of the bedform towards a linear lee side of the bedform.

At the hydraulic jump erosion is caused by high shear stresses and increased turbulence. High shear stress is explained by relatively high velocities near the bed in the hydraulic jump region (Fig. 4A and Fig. 5A1). Increased turbulence in this region, caused by coherent flow structures, allows sediment to remain in suspension and inhibits settling. The amount of sediment stored in the water column increases over the hydraulic jump region (Fig. 6D). As a result the morphological effect of the hydraulic jump is a transition from a steep and strongly erosive lee side, through a concave trough, and to a depositional upstream dipping stoss side.

In the subcritical flow region the sediment entrainment flux is smaller than that of sediment settling flux, as low bed shear stresses limit the entrainment. The low turbulence levels in the subcritical region causes the sediment picked up on the lee side to settle. Sediment grains collect at the base of the flow before settling (Fig. 6E), thereby causing flow stratification as a result of limited mixing. The morphological response to this depositional subcritical flow region is an increase in bed-elevation over the stoss side, with more sediment being deposited close to the trough than near the crest, effectively decreasing the topography between crest and trough, setting up the system to change to flow state 2.

Flow state 2 (B)

Observation (C)

In state 2, supercritical flow prevails over the entire bedform. Even though the flow thickens over the stoss side of the bedform towards the crest, the flow remains supercritical. The thicker supercritical flow on the stoss side is still depositional with excess shear stresses ranging from 5 to 7 Pa.

More sediment is deposited at the crest than in the trough in flow state 2, thereby increasing the topography (Fig. 7B). Such increased topography caused by deepening of the trough and deposition on the crest triggers the formation of a new hydraulic jump (Fig. 7B and C).

Interpretation (C)

In state 2 the lee side of the cyclic step remains erosive. Notwithstanding the supercritical flow conditions, the stoss side of the bedform is still depositional as the settling flux exceeds the sediment entrainment flux.

The morphological behaviour in state 2 is not unlike that of antidunes, because more sediment is deposited near the crest than at the trough the topography of the bedform to increases. When comparing the flow parameters with the bedform geometry through empirical equations of Kennedy (1960) and Alexander et al. (2011), it is clear that the bedforms are, however, not antidunes. An increase in topography in flow state 2 sets up the system to create a new hydraulic jump and return to flow state 1. The hydraulic jump forms at the crest of the bedforms and migrates towards the trough. This alteration between two flow states, with depositional patterns that inherently require an alteration from one state to another, is also described in a carbonate ramp setting which is interpreted to have backset beds formed by cyclic steps (Slootman et al. 2015). The cycle alternating between flow states 1 and 2 appears to be an autogenous interplay between bed topography and the flow, and is inherent to the depositional pattern of the two flow states.

Depositional signature (A)

Sedimentary structures can be indicative of palaeo-flow conditions and therefor provide an aide to reconstruct the palaeo-environment. Hence it is important to understand the formative processes of bedforms and their associated sedimentary structures. Here the modelling results are used to directly link the flow-process to the depositional product. The cyclic step simulations provide flow conditions at the moment of deposition for each subgridded sediment parcel at every time step, and hence the model not only builds up a series of sedimentary structures, but is also able to link the individual parts of these sedimentary structures with their flow conditions during deposition.

Discussed herein is the development of the depositional architecture (Fig. 8A to E) and the parameters that control the sedimentary facies. Supplementary video 2 visually complements the subsection regarding architecture. The discussed parameters are: (i) the sediment concentration near the bed (Fig. 8F); (ii) the flow regime, represented by Froude number (Fig. 8G); and (iii) the bed shear stress (Fig. 8H), an important factor in how erosive or depositional the flow is, and responsible for grain-size trends.

Architecture (B)

The architecture of the deposit associated with a cyclic step system is dependent on the rate of aggradation. In an aggradational system the architecture consists of upstream-dipping laminations ($<10^{o}$), called backsets, which form on the depositional stoss side of the bedform (Fig. 9A) (Kostic and Parker, 2006; Spinewine et al., 2009; Yokokawa et al., 2009; Lang and Winsemann, 2013). The backsets onlap onto a composite erosional surface at their upstream side, which forms the lower set-boundary. The backsets are truncated at their downstream side by a similar erosive surface, forming the upper set-boundary. The simulations in this study are not aggradational but transportational, this is reflected by a different depositional architecture (Fig. 9B). The resulting depositional architecture is an amalgamation of concave-up erosion surfaces and small portions of preserved low-angle backsets and foresets creating mostly concave-up lenticular bodies (Fig. 9B).

The development of the architecture of transportational cyclic steps in Fig. 9B is seen in Fig. 8A to E. A deep trough that formed during washout of the hydraulic jump is filled by sediment (Fig. 8B). The sediment laps onto the erosion surface as a foreset with a downstream transitions into a backset ($<5^{o}$). This creates a concave-up deposit (Fig. 8B). A large portion of the deposited backsets is eroded by the upslope migration of the successive bedform (Fig. 8A-E). The deposits shown in Fig. 8B are mostly reworked in Fig. 8C, and only the deepest trough infill near the initial onlap is preserved. These deepest trough deposits form below the hydraulic jump. If the flow is supercritical throughout (state 2), steeper backsets and more tabular backsets are formed (Fig. 8D). These steeper, tabular backsets (<10^{o}) are less likely to be preserved as they form near the crest, which is more prone to erosion. During the transition from state 2 (supercritical throughout), to state 1 (with hydraulic jump), erosion can occur on the stoss side, leading to upstream truncation of the laminations.

Sediment concentration (B)

The sediment concentration at the moment of deposition over a cyclic step (Fig. 8F) is generally lower than 9% by volume. Deposits that form under subcritical flow form at lower near-bed sediment concentration (*ca* 5%) than the deposits formed under supercritical flow (*ca* 8%) (Fig. 8F). The flow is generally dilute (<9 vol.%) in all regions (Fig. 5C), implying turbulence is the dominant grain support mechanism (Bagnold, 1954).

Flow regime (B)

Even though a cyclic step is characterised by supercritical flow over the lee side, the deposits are predominantly formed in the subcritical flow regime (Fig. 8G). Traces of bedforms associated with the subcritical flow regime, such as current ripples, superimposed on the larger scale bedform could therefore be formed as a consequence. Bedform stability diagrams indicate that flow over proximal backset deposits are within the ripple regime (Van den Berg and Van Gelder, 1993). Ripples have been associated with subcritical flow after a hydraulic jump in the distal part of hydraulic jump bars (Macdonald et al., 2013). Given the high settling rate following the hydraulic jump such current ripples could initially be climbing. Ripples are, however, not simulated in the numerical model due to a lack of resolution. Deposition during supercritical flow conditions (state 2) also result in a backset (Fig. 8G). Backsets deposited during supercritical flow onlap further downstream than those formed at subcritical conditions and are steeper.

Shear stress (B)

Cyclic step deposits show alternation in bed shear stress over time and space (Fig. 8H). Variability in shear stress over time would lead to a variation in grain size from one backset stratum to another, creating lamination, and thereby delineating individual backset strata. In general shear stresses at the moment of deposition decrease from trough to crest (Fig. 9B). Deposits that form directly after the rapid erosion, have lowest shear stresses as a roller forms below the main flow (20% of the time), see Fig. 9B. In the absence of a hydraulic jump, shear stresses over the stoss side are relatively high and there is increased traction on the bed where the deposits form (Fig 9B).

The simulations in this study show a decrease in shear stress over the stoss side of the bedform (Fig. 6C). Decrease in shear stress can create a downstream fining through a decrease of flow competence to carry sediment or due to a decrease in flow capacity to carry sediment. Submarine cyclic steps are also suggested to be downstream fining, but not due a decrease in shear stress, as shear stress is suggested to increase over the stoss side (Postma & Cartigny, 2014). The downstream fining, as described by Postma & Cartigny (2014), would be caused by a decrease in capacity of the flow to carry sediment. Both the capacity and competence argument can be used to explain downstream fining (Hiscott, 1994). Open-channel-flows and turbidity currents both can create cyclic steps, but are in many ways different, in velocity-profile and concentration profile to start with, and in shear stress pattern as a consequence. Both a decrease in flow capacity and a decrease in flow competence can produce downstream fining, and it is well possible that the two mechanisms play different roles in marine and fluvial systems, but ultimately lead to a similar result.

Consequences for outcrop studies (A)

Recognition of cyclic step deposits in outcrop is strongly dependent on the preservation potential of the deposits, and whether cyclic step systems are aggradational or transportational (Fig. 9). Deposits associated with strongly aggradational cyclic steps have a different depositional signature than deposits resulting from transportational cyclic steps.

A highly aggradational cyclic step system in outcrop may resemble the deposit such as seen in Fig. 9A, which represents an idealised deposit. There is a clear sequence of backsets that are separated by set boundaries at the upstream side and at the downstream side. Downstream fining within sets results in a normal grading in the vertical due to progressively upstream emplacement of the backsets. Such depositional signatures of aggradational cyclic step systems are, however, uncommon in fluvial outcrops, where clear sequences of continuously stacked backsets are absent due to a lack accommodation space. In marine and deltaic settings accommodation space is more readily available, and the character described above is observed in outcrop (Ventra et al., 2015; Dietrich et al., 2016) and in shallow seismic imagery (Migeon et al., 2000; Migeon et al., 2001; Normark et al., 2002; Fildani et al., 2006; Migeon et al., 2006; Flood et al., 2009; Gilbert and Crookshanks, 2009; Heinio and Davies, 2009; Zhong et al., 2015).

Cyclic steps that are transportational have a different depositional signature (Fig. 9B) than aggradational ones. The overall depositional signature is an amalgamation of lenticular bodies bound by erosion surfaces. Similar to the backsets formed in an aggradational setting, backsets formed in a transportational setting are downstream fining. The deposited backsets are reworked for a large part; on the downstream part by upstream migrating erosion, and on the upstream part when the hydraulic jump gets washed out. At the washout stage of a hydraulic jump the trough migrates upstream rapidly and erodes underlying sediments creating a deep new trough. Sediments deposited in this trough create a concave-up lens, with the best preservation potential of the flow as the trough cut deep into the substrate, out of reach of subsequent erosion. The concave-up bodies formed at low shear stress conditions, may be associated with suspension fallout due to a decrease in flow capacity. Backsets that form when the flow is supercritical throughout (state 2) are steepest, as they enhance the existing topography. These backsets also form under relatively high shear stress where there is traction on the bed, grain sizes in these backsets are likely to be larger than average as fines will not be able to settle at these conditions (decrease in flow competence). These transportational cyclic step deposits resemble those observed in small-scale laboratory experiments (Yokokawa et al., 2009).

When comparing the simulated depositional signature to signature in the geological record, it is important to appreciate differences of scale. Cyclic step facies have been interpreted in outcrops of deltaic settings (Dietrich et al., 2016) and glacial flood outbursts (Duller et al., 2008; Lang and Winsemann, 2013). In these settings concave-up troughs are filled with diffusely laminated backsets. The troughs are typically several metres long and the backsets within them vary in steepness between 5^{o} and 20^{o} (Lang and Winseman, 2013; Duller et al., 2008; Dietrich et al., 2016). In the numerical results show a very similar architecture, but on a smaller scale. Both in this study and in outcrop distinct concave-up troughs are filled by diffusely laminated foresets and backsets that dip 5^{o} to 15^{o} (Fig. 9B). Erosion surfaces in the simulations dip in the order of 5^{o} to 15^{o} (Fig. 9B), their abundance and the size of the preserved backsets is dependent on the rate of aggradation. The faint stratification described in Duller et al. (2008) and Lang and Winseman (2013), is probably due to a change in shear stress on the bed related to the stages in which the flow is supercritical throughout. Dietrich et al. (2016) show a series of upstream dipping backsets that are indicative of more aggradational cyclic steps, as these backsets are not cross-cut by an erosive surface but rather a more continuous stack of backsets such as seen in Fig. 9A. More aggradation yields fewer erosional surfaces as well as more preservation of backsets relative to foresets.

Conclusions (A)

The depth-resolved numerical model allows a unique insight into the mechanics of a cyclic step system, and the modelling results can be used to link the mechanics to the depositional signature. The simulated cyclic steps generally adhere to existing conceptual models, with Froude-supercritical flow over the lee side and Froude-subcritical flow over the stoss side of the bedform. The hydraulic jump affects a large flow region and is often itself erosive. A hydraulic jump is not always present, and the flow occasionally is only supercritical, but still deposits at the stoss side. In absence of a hydraulic jump the bedform amplitude is enhanced and leads to the formation of a new hydraulic jump.

The depositional signature of a cyclic step system is dependent on the rate of aggradation. In the case of high aggradation rate, a package of backsets, bound upstream and downstream by erosive surfaces, can be found. In more transportational systems, the deposited backsets will be reworked to a large degree. The depositional signature of cyclic steps is dominated by an amalgamation of concave-up erosional surfaces and low-angle foresets and backsets creating lenticular bodies. This depositional signature is determined to a large extent by the transient nature of the hydraulic jump as it migrates upstream and downstream with respect to the trough location, and is occasionally washed out entirely. Similar geometries are visible over a range of scales in outcrop studies. Variation in shear stress at the moment of deposition, likely related to presence or absence of a hydraulic jump, results in more pronounced backsets of a distinct grain size.

Acknowledgements (A)

ExxonMobil is acknowledged for funding this research. Riccardo Basani and Romain Rouzairol are thanked for their help and advice during the modelling phase of this study. Arnoud Slootman is acknowledged for fruitful discussions on the subject of cyclic step morphodynamics. Aaron Fricke, Pierre Dietrich, Svetlana Kostic and Jorg Lang are thanked for their valuable reviews that have improved the paper significantly.

References (A)

Alexander, J., 2008, Bedforms in Froude-supercritical flow, *in* Marine and River Dune Dynamics Proceedings, p. 1–5.

Alexander, J., Bridge, J.S., Cheela, R.J., and Leclair, S.F., 2001, Bedforms and associated sedimentary structures formed undersupercritical waterfows over aggrading sand beds.: *Sedimentology*, v. **48**, p. 133–152.

Babonneau, N., Delacourt, C., Cancourt, R., Sisavath, E., Bachelery, P., Mazuel, A., Jorry, S.J., Deschamps, A., Ammann, J., and Villeneuve, N., 2013, Direct sediment transfer from land to deep-sea: Insights into shallow multibeam bathymetry at La Reunion Island.: *Marine Geology*, v. **346**, p. 47–57.

Bagnold, R.A., 1954, Experiments on a gravity-free dispersion of large solid spheres in a Newtonian fluid under shear.: *Proceedings of the Royal Society of Londen. Series A, Mathematical and Physical Sciences*, v. **225**, p. 49–63.

Balmforth, N.J., and Vakil, a., 2012, Cyclic steps and roll waves in shallow water flow over an erodible bed.: *Journal of Fluid Mechanics*, v. **695**, p. 35–62.

Basani, R., Janocko, M., Cartigny, M.J.B., Hansen, W.M., and Eggenhuisen, J.T., 2014, MassFLOW-3D TM as a simulation tool for turbidity currents : some preliminary results.: *From Depositional Systems to Sedimentary Successions on the Norwegian Continental Margin (Special Publication 46 of the IAS) (Editors: Martiunus, A.W., Ravenas A., Howell, J.A., Steel, .R.J., Wonham, J.P.)*, v. **46**, p. 587–608.

Van den Berg, J.H., and Van Gelder, A., 1993, A new bedform stability diagram, with emphasis on the transition of ripples to plane bed in flows over fine sand and silt.: *Special Publication of the International Association of Sedimentologists 17 (Ed. M. Marzo, M. and Puigdefabregas, C.)*, v. **17**, p. 11–21.

Cartigny, M.J.B., Postma, G., van den Berg, J.H., and Mastbergen, D.R., 2011, A comparative study of sediment waves and cyclic steps based on geometries, internal structures and numerical modeling.: *Marine Geology*, v. **280**, p. 40–56.

Cartigny, M.J.B., Ventra, D., Postma, G., and van Den Berg, J.H., 2014, Morphodynamics and sedimentary structures of bedforms under supercritical-flow conditions: New insights from flume experiments.: *Sedimentology*, v. **61**, p. 712–748.

Covault, J.A., Kostic, S., Paull, C.K., Ryan, H.F., and Fildani, A., 2014, Submarine channel initiation, filling and maintenance from sea-floor geomorphology and morphodynamic modelling of cyclic steps.: *Sedimentology*, v. **61**, p. 1–24.

Covault, J.A., Kostic, S., Paull, C.K., Sylvester, Z., and Fildani, A., 2016, Cyclic steps and related supercritical bedforms: Building blocks of deep-water depositional systems, western North America.: *Marine Geology*, v. **in press**.

Dietrich, P., Ghienne, J.-F., Normandeau, A., and Lajeunesse, P., 2016, Upslope-Migrating Bedforms In A Proglacial Sandur Delta: Cyclic Steps From River-Derived Underflows?: *Journal of Sedimentary Research*, v. **86**, p. 113–123.

Duarte, J.C., Terrinha, P., Rosas, F.M., Valadares, V., Pinheiro, L.M., Matias, L., Magalhães, V., and Roque, C., 2010, Crescent-shaped morphotectonic features in the Gulf of Cadiz (offshore SW Iberia).: *Marine Geology*, v. **271**, p. 236–249.

Duller, R.A., Mountney, N.P., Russell, A.J., and Cassidy, N.C., 2008, Architectural analysis of a volcaniclastic jökulhlaup deposit, southern Iceland: sedimentary evidence for supercritical flow.: *Sedimentology*, v. **55**, p. 939–964.

Fagherazzi, S., and Sun, T., 2003, Numerical simulations of transportational cyclic steps.: *Computers & Geosciences*, v. **29**, p. 1143–1154.

Fielding, C.R., 2006, Upper flow regime sheets, lenses and scour fills: Extending the range of architectural elements for fluvial sediment bodies.: *Sedimentary Geology*, v. **190**, p. 227–240.

Fielding, C.R., Allen, J.P., Alexander, J., and Gibling, M.R., 2009, Facies model for fluvial systems in the seasonal tropics and subtropics.: *Geology*, v. **37**, p. 623–626.

Fildani, A., Normark, W.R., Kostic, S., and Parker, G., 2006, Channel formation by flow stripping: large-scale scour features along the Monterey East Channel and their relation to sediment waves.: *Sedimentology*, v. **53**, p. 1265–1287.

Flood, R.D., Hiscott, R.N., and Aksu, A.E., 2009, Morphology and evolution of an anastomosed channel network where saline underflow enters the Black Sea.: *Sedimentology*, v. **56**, p. 807–839.

Foley, M.G., 1977, a Quantitative Hydrodynamic Indicator I.: *Journal of sedimentary petrology*, v. **47**, p. 738–746.

Fricke, A.T., Sheets, B.A., Nittrouer, C.A., Allison, M.A., and Ogston, A.S., 2015, An examination of Froude-supercritical flows and cyclic steps on a subaqeous lacustrine delta, Lake Chelan, Washington, U.S.A.: *Journal of Sedimentary Research*, v. **85**, p. 754–767.

Ge, Z., Nemec, W., Gawthorpe, R.L., and Hansen, E.W.M., 2017, Response of unconfined turbidity current to normal-fault topography.: *Sedimentology*, v. **64**, p. 1–28.

Ghienne, J.-F., Girard, F., Moreau, J., and Rubino, J.-L., 2010, Late Ordovician climbing-dune cross-stratification: a signature of outburst floods in proglacial outwash environments?: *Sedimentology*, v. **57**, p. 1175–1198.

Gilbert, R., and Crookshanks, S., 2009, Sediment waves in a modern high-energy glacilacustrine environment.: *Sedimentology*, v. **56**, p. 645–659.

Guo, J., 2002, Hunter Rouse and Shields diagram.: *Advances in Hydraulic and Water Engineering*, v. **2**, p. 1096–1098.

Heinio, P., and Davies, R.J., 2009, Trails of depressions and sediment waves along submarine channels on the continental margin of Espirito Santo Basin, Brazil.: *Geological Society of America Bulletin*, v. **121**, p. 698–711.

Hiscott, R.N., 1994, Loss of capacity, not competence, as the fundamental process governing deposition from turbidity currents.: *Journal of Sedimentary Research*, v. **64**, p. 203–214.

Hughes Clarke, J.E., Brucker, S., Muggah, J., Hamilton, T., Cartwright, D., Church, I., and Kuus, P., 2012, Temporal progression and spatial extent of mass wasting events on the Squamish prodelta slope, *in* Al., E. et ed., Landslides and Engineered Slopes: Protecting Society trhrough Improved Understanding, Taylor & Francis Group, London, p. 1091–1096.

Jobe, Z.R., Lowe, D.R., and Uchytil, S.J., 2011, Two fundamentally different types of submarine canyons along the continental margin of Equatorial Guinea.: *Marine and Petroleum Geology*, v. **28**, p. 843–860.

Jorritsma, 1973, Sluiting tijdelijke toegang Europoort - onderzoek naar de taludhellingen onder water aangebracht zand - verslag model onderzoek: Waterloopkundig Laboratorium.

Kennedy, J.F., 1969, The Formation of Sediment Ripples, Dunes, and Antidunes.: *Annual Review of Fluid Mechanics*, v. **1**, p. 147–168.

Kostic, S., 2011, Modeling of submarine cyclic steps: Controls on their formation, migration, and architecture.: *Geosphere*, v. **7**, p. 294–304.

Kostic, S., 2014, Upper flow regime bedforms on levees and continental slopes: Turbidity current flow dynamics in response to fine-grained sediment waves.: *Geosphere*, v. **10**, p. 1094–1103.

Kostic, S., and Parker, G., 2006, The response of turbidity currents to a canyon–fan transition: internal hydraulic jumps and depositional signatures.: *Journal of Hydraulic Research*, v. **44**, p. 631–653.

Kostic, S., Sequeiros, O., Spinewine, B., and Parker, G., 2010, Cyclic steps: A phenomenon of supercritical shallow flow from the high mountains to the bottom of the ocean.: *Journal of Hydro-environment Research*, v. **3**, p. 167–172.

Lamb, M.P., Parsons, J.D., Mullenbach, B.L., Finlayson, D.P., Orange, D.L., and Nittrouer, C. a., 2008, Evidence for superelevation, channel incision, and formation of cyclic steps by turbidity currents in Eel Canyon, California.: *Geological Society of America Bulletin*, v. **120**, p. 463–475.

Lang, J., and Winsemann, J., 2013, Lateral and vertical facies relationships of bedforms deposited by aggrading supercritical flows: From cyclic steps to humpback dunes.: *Sedimentary Geology*, v. **296**, p. 36–54.

Macdonald, R.G., Alexander, J., Bacon, J.C., and Cooker, M.J., 2013, Variations in the architecture of hydraulic-jump bar complexes on non-eroding beds. (S. Dey, Ed.): *Sedimentology*, v. **60**, p. 1291–1312.

Maier, K.L., Fildani, A., Paull, C.K., McHargue, T.R., Graham, S. a., and Caress, D.W., 2013, Deep-sea channel evolution and stratigraphic architecture from inception to abandonment from high-resolution Autonomous Underwater Vehicle surveys offshore central California.: *Sedimentology*, v. **60**, p. 935–960.

Mastbergen, D.R., and Van Den Berg, J.H., 2003, Breaching in fine sands and the generation of sustained turbidity currents in submarine canyons.: *Sedimentology*, v. **50**, p. 625–637.

Meyer-Peter, E. and Müller, R., 1948, Formulas for Bed-Load Transport, *in* International Association for Hydraulic Structures Research, p. 38–64.

Middleton, G. V, 1965, Antidune cross-bedding in a large flume.: *Journal of sedimentary petrology*, v. **35**, p. 922–927.

Migeon, S., Mulder, T., Savoye, B., and Sage, F., 2006, The Var turbidite system (Ligurian Sea, northwestern Mediterranean)—morphology, sediment supply, construction of turbidite levee and sediment waves: implications for hydrocarbon reservoirs.: *Geo-Marine Letters*, v. **26**, p. 361–371.

Migeon, S., Savoye, B., and Faugeres, J.-C., 2000, Quaternary development of migrating sediment waves in the Var deep-sea fan: distribution, growth pattern, and implication for levee evolution.: *Sedimentary Geology*, v. **133**, p. 265–293.

Migeon, S., Savoye, B., Zanella, E., Mulder, T., Faug??res, J.C., and Weber, O., 2001, Detailed seismic-reflection and sedimentary study of turbidite sediment waves on the var sedimentary ridge (SE France): Significance for sediment transport and deposition and for the mechanisms of sediment-wave construction.: *Marine and Petroleum Geology*, v. **18**, p. 179–208.

Nordin, C.F., and Beverage, J.P., 1965, Sediment Transport in the Rio Grande New Mexico: US Government Printing Office.

Normandeau, A., Lajeunesse, P., G.Poiré, A., and Francus, P., 2016, Morphological expression of bedforms formed by supercritical sediment density flows in four fjord-lake deltas of the south-eastern Canadian Shield (Eastern Canada).: *Sedimentology*, v. **63**, p. 2106–2129.

Normark, W.R., Piper, D.J.W., Posamentier, H., Pirmez, C., and Migeon, S., 2002, Variability in form and growth of sediment waves on turbidite channel levees.: *Marine Geology*, v. **192**, p. 23–58.

Parker, G., 1996, Coherent flow structures in open channels (P. J. Ashworth, S. J. Bennett, J. L. Best, & S. J. McLelland, Eds.): John Wiley and Sons Ltd., London.

Parker, G., 2008, Cyclic steps: A phenomenon of supercritical shallow flow from the high mountains to the bottom of the ocean, *in* 2nd International symosium on shallow flows,.

Parker, G., and Izumi, N., 2000, Purely erosional cyclic and solitary steps created by flow over a cohesive bed.: *Journal of Fluid Mechanics*, v. **419**, p. 203–238.

Paull, C.K., Ussler III, W., Caress, D.W., Lundsten, E., Covault, J. a., Maier, K.L., Xu, J., and Augenstein, S., 2010, Origins of large crescent-shaped bedforms within the axial channel of Monterey Canyon, offshore California.: *Geosphere*, v. **6**, p. 755–774.

Ponce, J.J., and Carmona, N., 2011, Coarse-grained sediment waves in hyperpycnal clinoform systems, Miocene of the Austral foreland basin, Argentina.: *Geology*, v. **39**, p. 763–766.

Postma, G., Cartigny, M., and Kleverlaan, K., 2009, Structureless, coarse-tail graded Bouma Ta formed by internal hydraulic jump of the turbidity current?: *Sedimentary Geology*, v. **219**, p. 1–6.

Postma, G., Kleverlaan, K., and Cartigny, M.J.B., 2014, Recognition of cyclic steps in sandy and gravelly turbidite sequences, and consequences for the Bouma facies model.: *Sedimentology*, v. **61**, p. 2268–2290.

Van Rijn, L.C., 1984, Sediment transport Part I Bed load transport.: *Journal of Engineering Mechanics*, v. **110**, p. 1431–1456.

Rouse, H., 1936, Discharge Characteristics of the Free Overfall: Use of Crest Section as a Control Provides Easy Means of Measuring Discharge.: *Civil Engineering*, v. **6**, p. 257–260.

Sequeiros, O.E., Spinewine, B., Garcia, M.H., Beaubouef, R.T., Sun, T., Savoye, B., and Parker, G., 2009, Experiments on Wedge-Shaped Deep Sea Sedimentary Deposits in Minibasins and/or on Channel Levees Emplaced by Turbidity Currents. Part I. Documentation of the flow.: *Journal of Sedimentary Research*, v. **79**, p. 593–607.

Slootman, A., Cartigny, M.J.B., Moscariello, A., Chiaradia, M., and de Boer, P.L., 2016, Quantification of tsunami-induced flows on a Mediterranean carbonate ramp reveals catastrophic evolution.: *Earth and Planetary Science Letters*, v. **444**, p. 192–204.

Soulsby, R., 1997, Dynamics of marine sands: a manual for practical applications: Thomas Telford, London.

Spinewine, B., Sequeiros, O.E., Garcia, M.H., Beaubouef, R.T., Sun, T., Savoye, B., and Parker, G., 2009, Experiments on wedge-shaped deep sea sedimentary deposits in minibasins and/or on chennel levees emplaced by turbidty currents. Part II.: *Journal of Sedimentary Research*, v. **79**, p. 608–628.

Sun, T., and Parker, G., 2005, Transportational cyclic steps created by flow over an erodible bed. Part 2. Theory and numerical simulation.: *Journal of Hydraulic Research*, v. **43**, p. 502–514.

Symons, W.O., Sumner, E.J., Talling, P.J., Cartigny, M.J.B., and Clare, M.A., 2016, Large-scale sediment waves and scours on the modern seafloor and their implications for the prevalence of supercritical flows.: *Marine Geology*, v. **371**, p. 130–148.

Taki, K., and Parker, G., 2005, Transportational cyclic steps created by flow over an erodible.: *Journal of Hydraulic Research*, v. **43**, p. 488–501.

Tubau, X., Paull, C.K., Lastras, G., Caress, D.W., Canals, M., Lundsten, E., Anderson, K., Gwiazda, R.,

and Amblas, D., 2015, Submarine canyons of Santa Monica Bay , Southern California : Variability in morphology and sedimentary processes.: *Marine Geology*, v. **365**, p. 61–79.

Ventra, D., Cartigny, M.J.B., Bijkerk, J.F., and Acikalin, S., 2015, Supercritical-flow structures on a Late Carboniferous delta front: Sedimentologic and paleoclimatic significance.: *Geology*, v. **43**, p. G36708.1.

Winterwerp, J.C., de Groot, M.B., Masebrgens, D.R., and Verwoert, H., 1992, Hyperconcentrated sand-water mixutre flows over erodible bed.: *Journal of Hydraulic Engineering*, v. **118**, p. 1508–1525.

Wong, M., and Parker, G., 2006, Reanalysis and Correction of Bed-Load Relation of Meyer-Peter and Müller Using Their Own Database.: *Journal of Hydraulic Engineering*, v. **132**, p. 1159–1168.

Wynn, R.B., and Stow, D.A. V, 2002, Classification and characterisation of deep-water sediment waves.: *Marine Geology*, v. **192**, p. 7–22.

Yagishita, K., and Taira, A., 1989, Grain fabric of a laboratory antidune.: *Sedimentology*, v. **36**, p. 1001–1005.

Yokokawa, M., Okuno, K., Nakamura, A., Muto, T., Miyata, Y., and Naruse, H., 2009, Aggradational cyclic steps: Sedimentary structures found in flume experiments.: *Proceedings 33rd IAHR Congress, Vancouver*, v. **81**, p. 5547–5554.

Zhong, G., Cartigny, M.J.B., Kuang, Z., and Wang, L., 2015, Cyclic steps along the South Taiwan Shoal and West Penghu submarine canyons on the northeastern continental slope of the South China Sea.: *Geological Society of America Bulletin*, v. **127**, p. 804–824.

Table captions

Table 1

Details on the generated mesh of the simulated domain

Table 2

Details on parameterisation of the simulations

[a] Based on Mastbergen & Van Den Berg, 2003

[b] Meyer-Peter and Muller relation, value based on Wong & Parker, (2006)

[c] Based on FLOW-3D release notes and manual

Table 3

Comparison Froude numbers and migration period of experimental and numerical results

Figure captions

Fig. 1

A schematic drawing of a cyclic step system. The stoss-side of the cyclic step is associated with a subcritical ($Fr < 1$) and depositional flow. The lee-side of cyclic step bedform is characterized by supercritical ($Fr > 1$) and erosive flow. The transition between supercritical and subcritical flow is marked by a hydraulic jump.

Fig. 2

The model setup as used for the simulations, flow over the bed is from left to right. The experimental setup used in Cartigny et al. (2014) has a similar geometry. The packed sediment bed is indicated in red, non-erodible components are indicated in blue.

Fig. 3

Time series comparison between the experimental results of Cartigny et al. (2013), run 9, and numerical simulation 1 of this study. The point of reference is a stationary location in the flume, as the sediment waves migrate a time-series is created. (A) The bed-surface and free-surface elevation time-series in the laboratory experiment. (B) The bed-surface and free-surface elevation in the numerical simulation. (C) The Froude numbers of the experimental observations (D) The Froude numbers of the numerical simulation in this study.

Fig. 4

Snapshots of the flow conditions in a cyclic step system, please note 2x vertical exaggeration in the figures. (A) The downstream-velocity field over a cyclic step. (B) The sediment concentration over a cyclic step. (C) The turbulent kinetic energy over a cyclic step. (D) The excess shear stresses over a cyclic step in Pa (black dots), fitted with a 5 pt. moving average curve in red.

Fig. 5

Profiles through the flow, one cyclic step wavelength (A), based on time-series data, showing downstream velocity (B), sediment concentration in (C) and turbulent kinetic energy (D).

Fig. 6

Six time-series plots of different physical properties over a cyclic step during one migration period. The properties are median or average properties based on 12 individual cyclic steps. One full migration period is displayed on the x-axis (0-1). The graphs display: (A) average bed elevation and free-surface elevation; (B) median Froude number; (C) median shear stress; (D) median depth-integrated (cumulative) sediment mass; (E) median near-bed sediment concentration, where near-bed is defined as the two computational cells closest to the bed; (F) median downstream sediment flux (sediment discharge).

Fig. 7

Five panels showing the flow behaviour during different stages of the cyclic step system, also shown are the associated newly formed deposits. The lines in the newly formed deposit are two-second timelines.

Fig. 8

Panels (A) to (E) show the development of the depositional architecture of a transportational cyclic step system at 50 second time intervals, with 10 second 10 time-lines within these intervals. Panels (F) to (H) display near-bed sediment concentration, Froude number, and shear stress at the moment a sediment parcel got deposited.

Fig. 9

Depositional architectures of aggradational cyclic steps (A) and more transportational cyclic steps (B). The figure also shows the inferred flow regime at which the deposits got formed. Please note that the black lines are time-lines, and not necessarily laminations due to grain-size breaks.

Tables

Table 1

Direction	Size	Number of cells	Cell size (minimum – maximum)
x	12.0 m	360	3.0 cm
y	0.15m	3	5.0 cm
z	1.0 m	38	1.8 cm – 8.5 cm

Table 2

Simulation	Specific discharge (m^2/s)	sediment concentration at inlet (vol %)	Entrainment coefficient[a]	Bed-load coefficient[b]	Drag coefficient	Angle of repose (deg)	Packing fraction	Initial bed inclinatio (deg)	Turbulent length scale (m)
1	0.77	5.6	0.018	4[b]	1	32	0.64	0.5	0.01[c]
2	0.93	5.6	0.018	4[b]	1	32	0.64	0.5	0.01[c]

Table 3

Simulation / Experiment	Fr_{50}	Fr_{90}	Period migration (s)
Experimental Run 9	1.15	2.07	85
Simulation 1	1.46 (+21%)	2.25 (+9%)	109 (+30%)
Experimental Run 15	1.31	2.06	n/a
Simulation 2	1.39 (+6%)	2.21 (+7%)	118

Appendix (A)

I: Governing equations RANS and turbulence models

Mass balance equation:

$$\frac{\partial \rho}{\partial t}+\frac{\partial}{dx}(\rho u)+\frac{\partial}{dy}(\rho v)+\frac{\partial}{dz}(\rho w)=0 \tag{1.1}$$

Momentum Balance equations:

$$\frac{\partial u}{\partial t}+u\frac{\partial u}{\partial x}+v\frac{\partial u}{\partial y}+w\frac{\partial u}{\partial x}=-\frac{1}{\rho}\frac{\partial p}{\partial x}+G_x+f_x \tag{1.2}$$

$$\frac{\partial v}{\partial t}+u\frac{\partial v}{\partial x}+v\frac{\partial v}{\partial y}+w\frac{\partial v}{\partial x}=-\frac{1}{\rho}\frac{\partial p}{\partial y}+G_y+f_y \tag{1.3}$$

$$\frac{\partial w}{\partial t}+u\frac{\partial w}{\partial x}+v\frac{\partial w}{\partial y}+w\frac{\partial w}{\partial x}=-\frac{1}{\rho}\frac{\partial p}{\partial z}+G_z+f_z \tag{1.4}$$

Turbulent kinetic energy balance:

$$\frac{\partial k_T}{\partial t}+\left(u\frac{\partial k_T}{\partial x}+v\ \frac{\partial k_T}{\partial y}+w\ \frac{\partial k_T}{\partial z}\right)=\ \ P_T+D_K-\varepsilon_T \tag{1.5}$$

Turbulent dissipation balance:

$$\frac{\partial \varepsilon_T}{\partial t}+\left(u\frac{\partial \varepsilon_T}{\partial x}+v\ \frac{\partial \varepsilon_T}{\partial y}+w\ \frac{\partial \varepsilon_T}{\partial z}\right)=\ \ \frac{C_{\varepsilon 1}\,\varepsilon_T}{k_T}P_T+D_\varepsilon-C_{\varepsilon 2}\frac{\varepsilon_T^2}{k_T} \tag{1.6}$$

From turbulence to dynamic viscosity:

$$v_T=0.085\frac{k_T^2}{\varepsilon_T} \tag{1.7}$$

$$\mu=\rho(\nu_m+\nu_t) \tag{1.8}$$

Further details on the k-epsilon RNG turbulence model van be found in (Basani et al., 2014).

II: Equations governing sediment transport model (B)

Shields numbers:

$$\theta=\frac{\tau}{gd(\rho_s-\rho_f)} \tag{2.1}$$

$$\theta_{cr}=\frac{0.3}{1+1.2d_*}+0.55(1-e^{-0.02d*}) \tag{2.2}$$

$$d_*=d\left(\frac{g(\rho_s/\rho_f-1)}{\nu_f}\right)^{1/3} \tag{2.3}$$

$$\theta'_{cr}=\theta_{cr}\frac{\cos(\psi)\sin(\chi)+\sqrt{\cos^2(\chi)\tan^2(\omega)-\sin^2(\psi)\sin^2(\chi)}}{\tan(\varphi)} \tag{2.4}$$

Bed load transport:

$$q_b = f_s \beta (\theta_i - \theta_{cr})^{1.5} \left[g \left(\frac{\rho_s - \rho_f}{\rho_f} \right) d_s^3 \right]^{\frac{1}{2}} \quad (2.5)$$

$$\delta = d \left[0.3 d_*^{0.7} ({}^{\theta}/_{\theta_{cr}} - 1)^{0.5} \right] \quad (2.6)$$

$$\boldsymbol{u_{bedload}} = \frac{q_b}{\delta} \frac{\overline{\boldsymbol{u}}}{\|\overline{\boldsymbol{u}}\|} \quad (2.7)$$

Suspended load transport:

$$\boldsymbol{u_{lift}} = \alpha_i n_s d_*^{0.3} (\theta_i - \theta_{cr})^{1.5} \sqrt{\frac{\|g\| d (\rho_s - \rho_f)}{\rho_f}} \quad (2.8)$$

$$\boldsymbol{u_{settle}} = \frac{\boldsymbol{g}}{g} \left[(10.36^2 + 1.049 d_*^3)^{1/2} - 10.36 \right] \frac{\nu_f}{d} \quad (2.9)$$

$$\boldsymbol{u_s} = \overline{\boldsymbol{u}} + \boldsymbol{u_{settle}} c_{vol} \quad (2.10)$$

$$\frac{\partial C}{\partial t} + \nabla \cdot (\boldsymbol{u_s} C_{mass}) = \nabla \cdot \nabla (D C_{mass}) \quad (2.11)$$

$$D = \frac{RMSC \cdot \mu}{\rho_f} + \frac{CMSC}{\rho_f} \quad (2.12)$$

$$c_{vol} = \frac{C_{mass}}{\rho_s} \quad (2.13)$$

II: List of symbols (B)

$A_{x,y,z}$	Fractional area
C_{mass}	Suspended sediment mass-concentration
C_{vol}	Suspended sediment volume concentration
CMSC	Coefficient of diffusion
$C_{\varepsilon1,\varepsilon2}$	Dimensionless parameter
D	Diffusion coefficient
D_K	Turbulent kinetic energy diffusion term
D_ε	Diffusion of dissipation of turbulence term
d	Grain size
d_*	Dimensionless grain parameter

$f_{x,y,z}$	Viscous accelerations
Fr	Froude number
g	Gravitational acceleration
$G_{x,y,z}$	Body accelerations
k_T	Turbulent kinetic energy
P_T	Turbulent kinetic energy production term
q_b	Bed-load transport rate
RMSC	Inverse Schmidt number
$\mathbf{u}_s$	Velocity of the suspended sediment
$\bar{\boldsymbol{u}}$	Mean velocity of water-sediment mixture, obtained via Navier-Stokes
$\mathbf{u}_{\mathbf{lift}}$	Lift velocity
$\mathbf{u}_{\mathbf{bedload}}$	Bed-load velocity
$\mathbf{u}_{\mathbf{settle}}$	Sediment settling mass-flux
α	Entrainment coefficient
β	Bed-load coefficient
δ	Thickness bed-load layer
ε_T	Turbulent dissipation
θ	Local Shields number
θ_{cr}	Critical Shields number
μ	Dynamic viscosity
ν_f	Kinematic viscosity of water
ρ_s	Density of the sediment
ρ_f	Density of the fluid
$\bar{\rho}$	Mean density fluid-sediment mixture
τ	Shear stress
τ_{cr}	Critical shear stress
χ	Angle slope of bed
ψ	Angle between flow and upslope direction
ω	Angle of repose

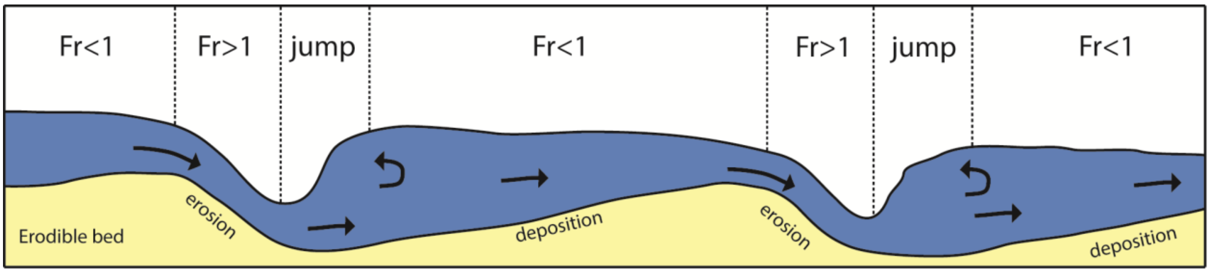
Fr<1
Fr>1
jump
Fr<1
Fr>1
jump
Fr<1
Erodible bed
erosion
deposition
erosion
deposition

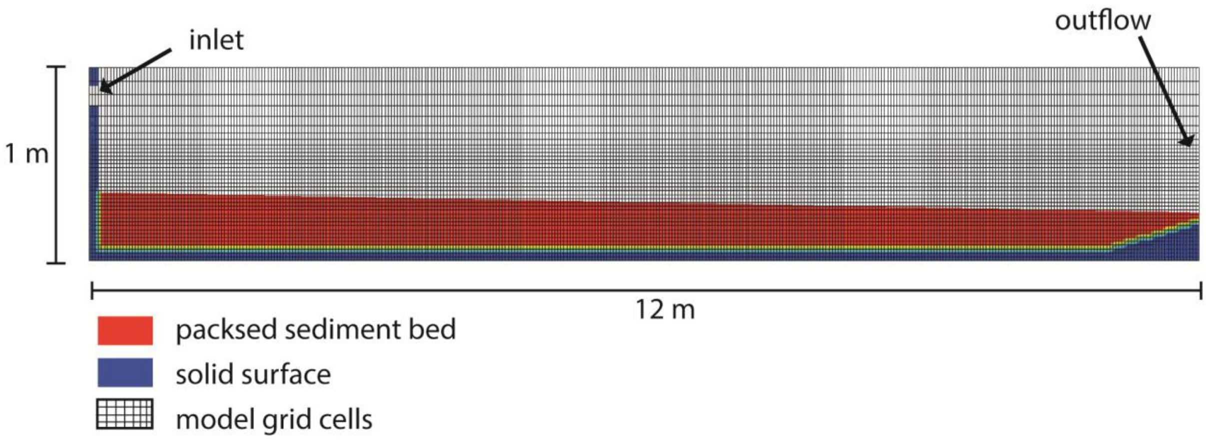
inlet
outflow
1 m
12 m
packsed sediment bed
solid surface
model grid cells

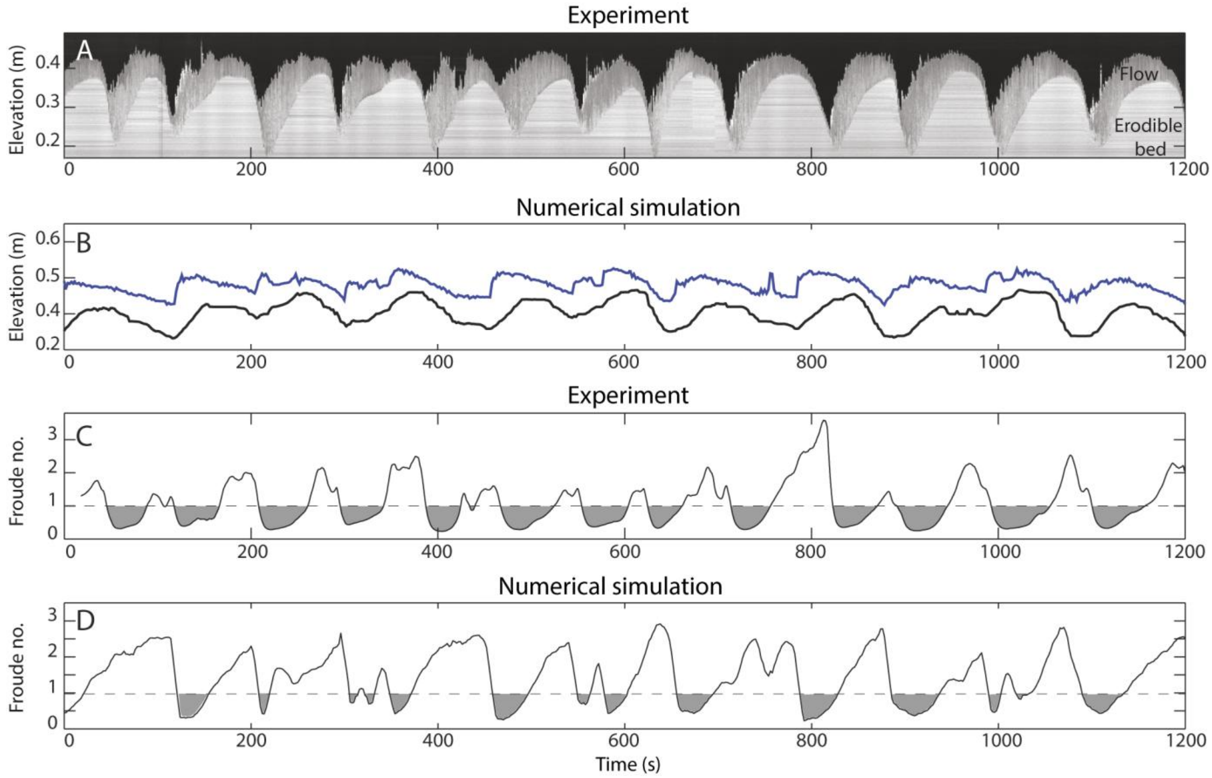

Experiment
A
Elevation (m)
0.4
0.3
0.2
Flow
Erodible bed
0
200
400
600
800
1000
1200
Numerical simulation
B
Elevation (m)
0.6
0.5
0.4
0.3
0.2
Experiment
C
Froude no.
3
2
1
0
Numerical simulation
D
Froude no.
Time (s)

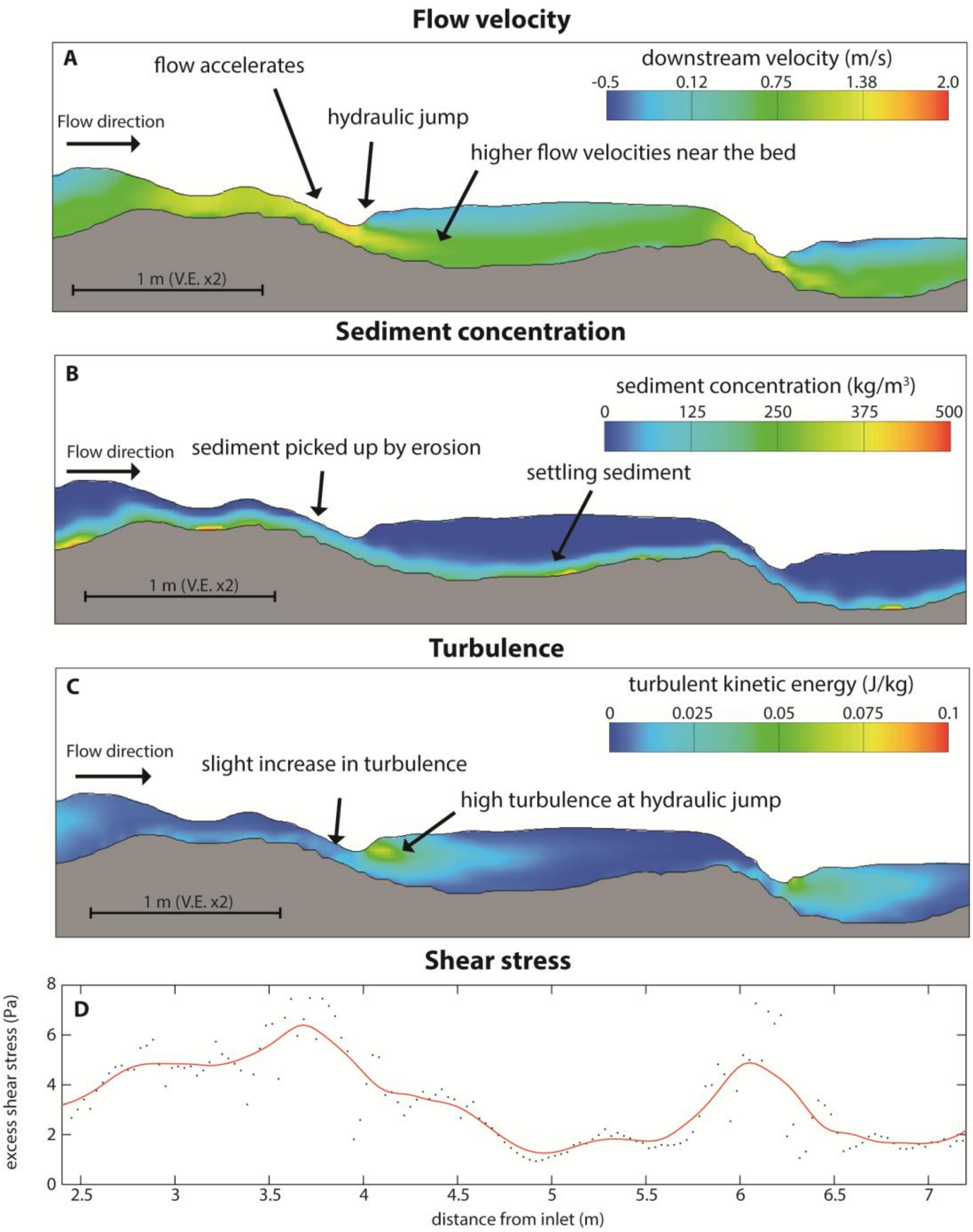

Flow velocity
A
flow accelerates
downstream velocity (m/s)
-0.5
0.12
0.75
1.38
2.0
Flow direction
hydraulic jump
higher flow velocities near the bed
1 m (V.E. x2)
Sediment concentration
B
sediment concentration (kg/m3)
0
125
250
375
500
Flow direction
sediment picked up by erosion
settling sediment
1 m (V.E. x2)
Turbulence
C
turbulent kinetic energy (J/kg)
0
0.025
0.05
0.075
0.1
Flow direction
slight increase in turbulence
high turbulence at hydraulic jump
1 m (V.E. x2)
Shear stress
D
excess shear stress (Pa)
0
2
4
6
8
2.5
3
3.5
4
4.5
5
5.5
6
6.5
7
distance from inlet (m)

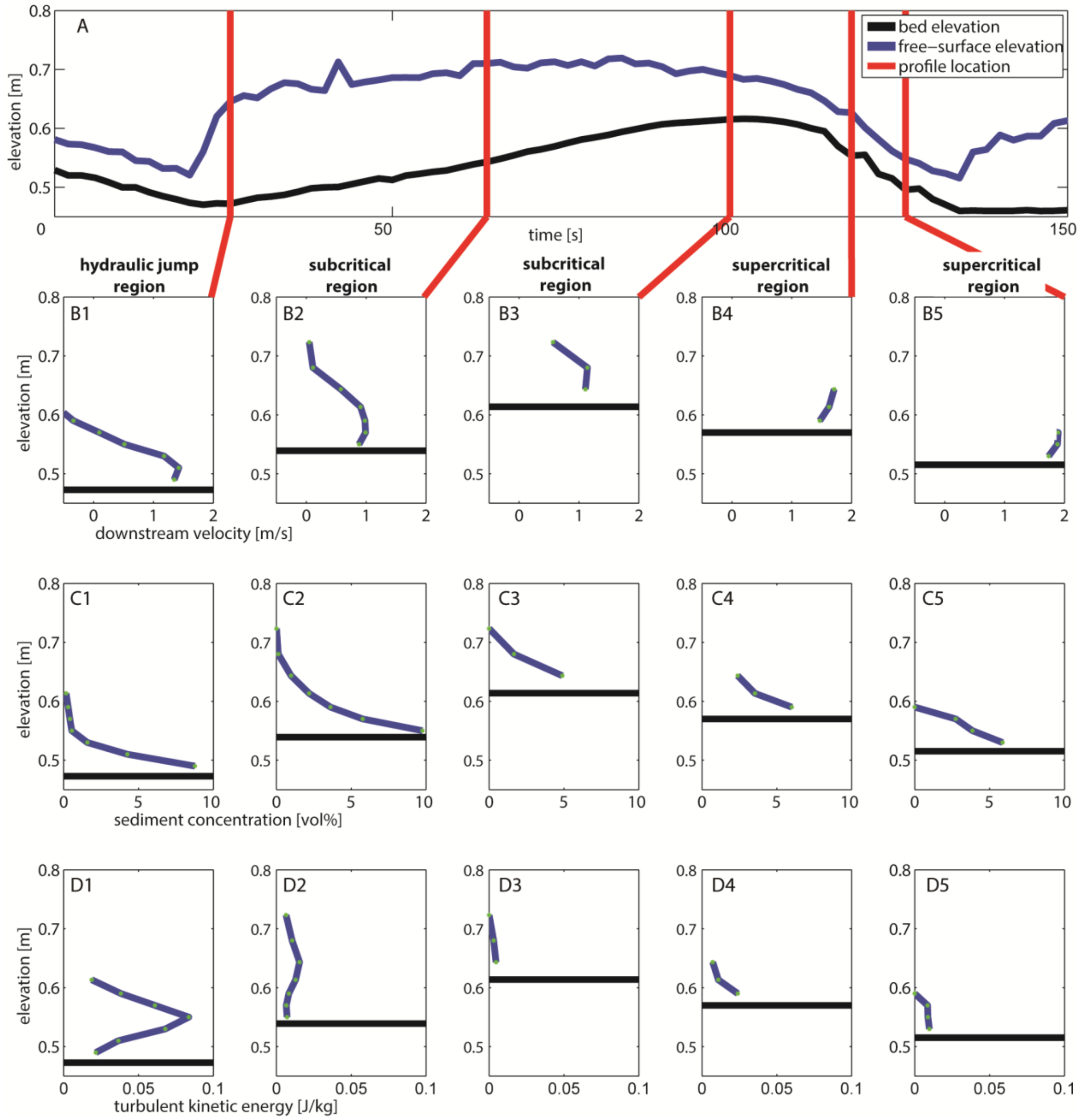
A
bed elevation
free−surface elevation
profile location
elevation [m]
time [s]
hydraulic jump region
subcritical region
subcritical region
supercritical region
supercritical region
B1
B2
B3
B4
B5
downstream velocity [m/s]
C1
C2
C3
C4
C5
sediment concentration [vol%]
D1
D2
D3
D4
D5
turbulent kinetic energy [J/kg]

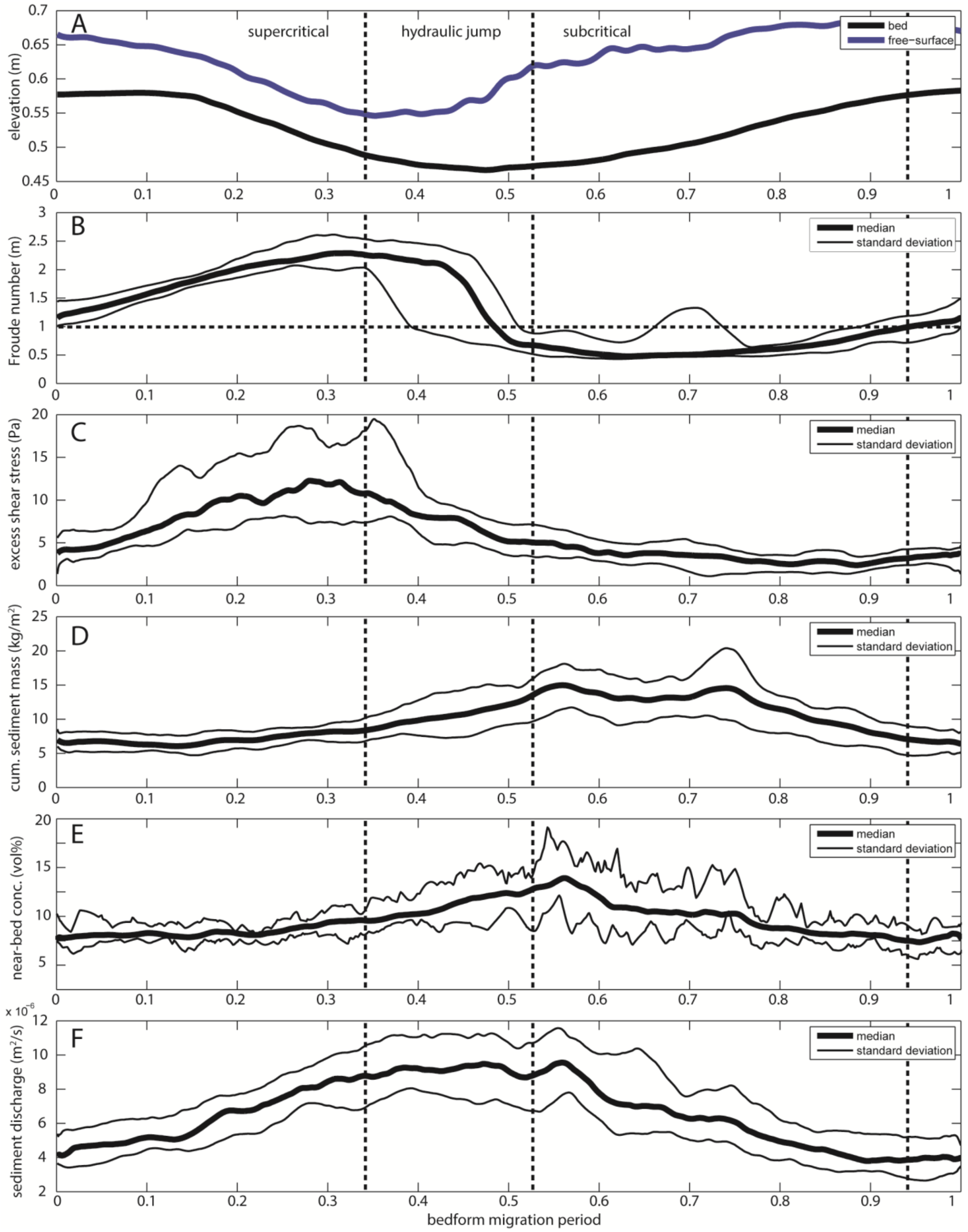
A
supercritical
hydraulic jump
subcritical
bed
free-surface
elevation (m)
B
median
standard deviation
Froude number (m)
C
excess shear stress (Pa)
D
cum. sediment mass (kg/m²)
E
near-bed conc. (vol%)
F
x 10⁻⁶
sediment discharge (m²/s)
bedform migration period

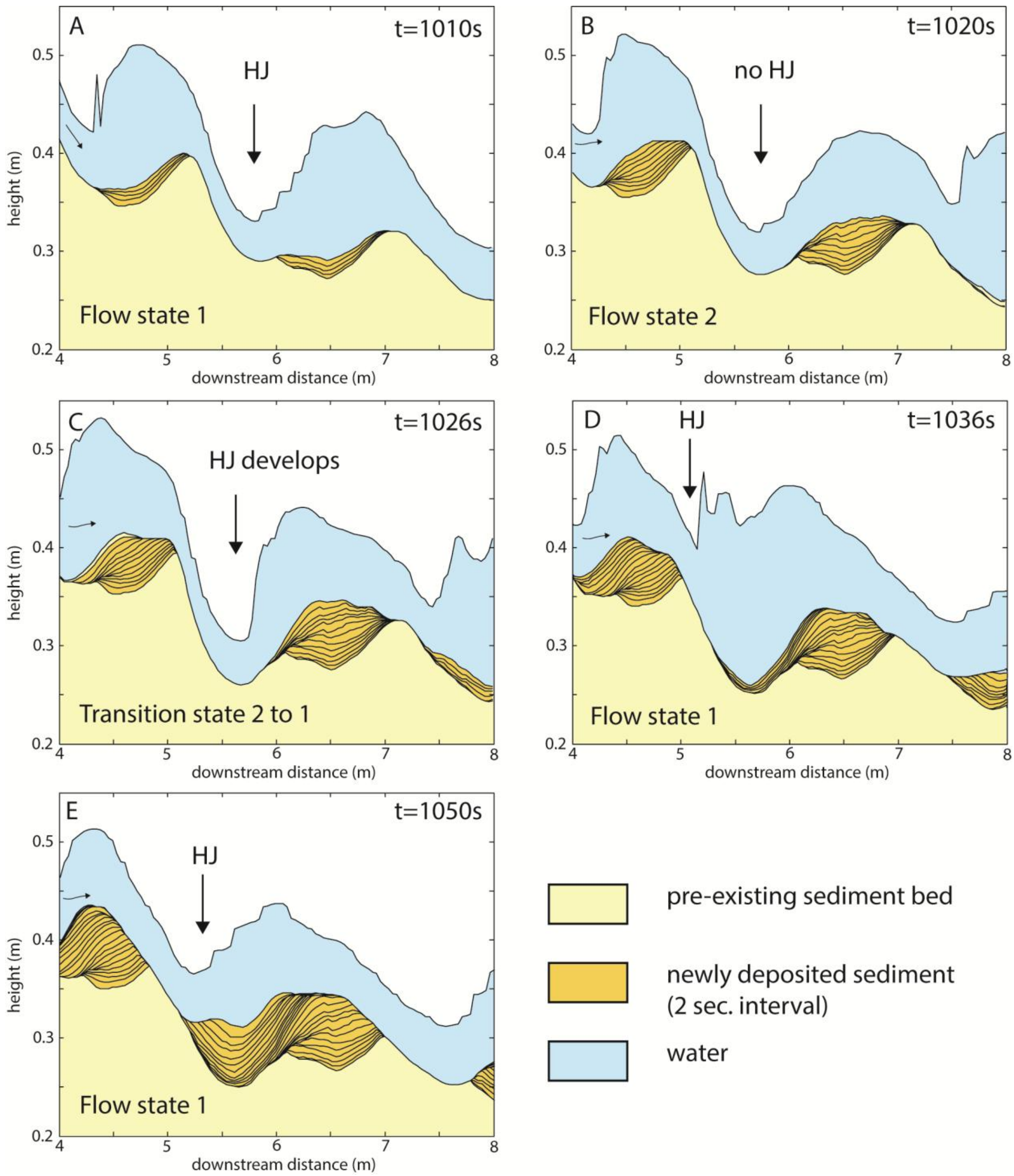
A
t=1010s
HJ
Flow state 1
B
t=1020s
no HJ
Flow state 2
C
t=1026s
HJ develops
Transition state 2 to 1
D
HJ
t=1036s
Flow state 1
E
t=1050s
HJ
Flow state 1
height (m)
downstream distance (m)
pre-existing sediment bed
newly deposited sediment
(2 sec. interval)
water

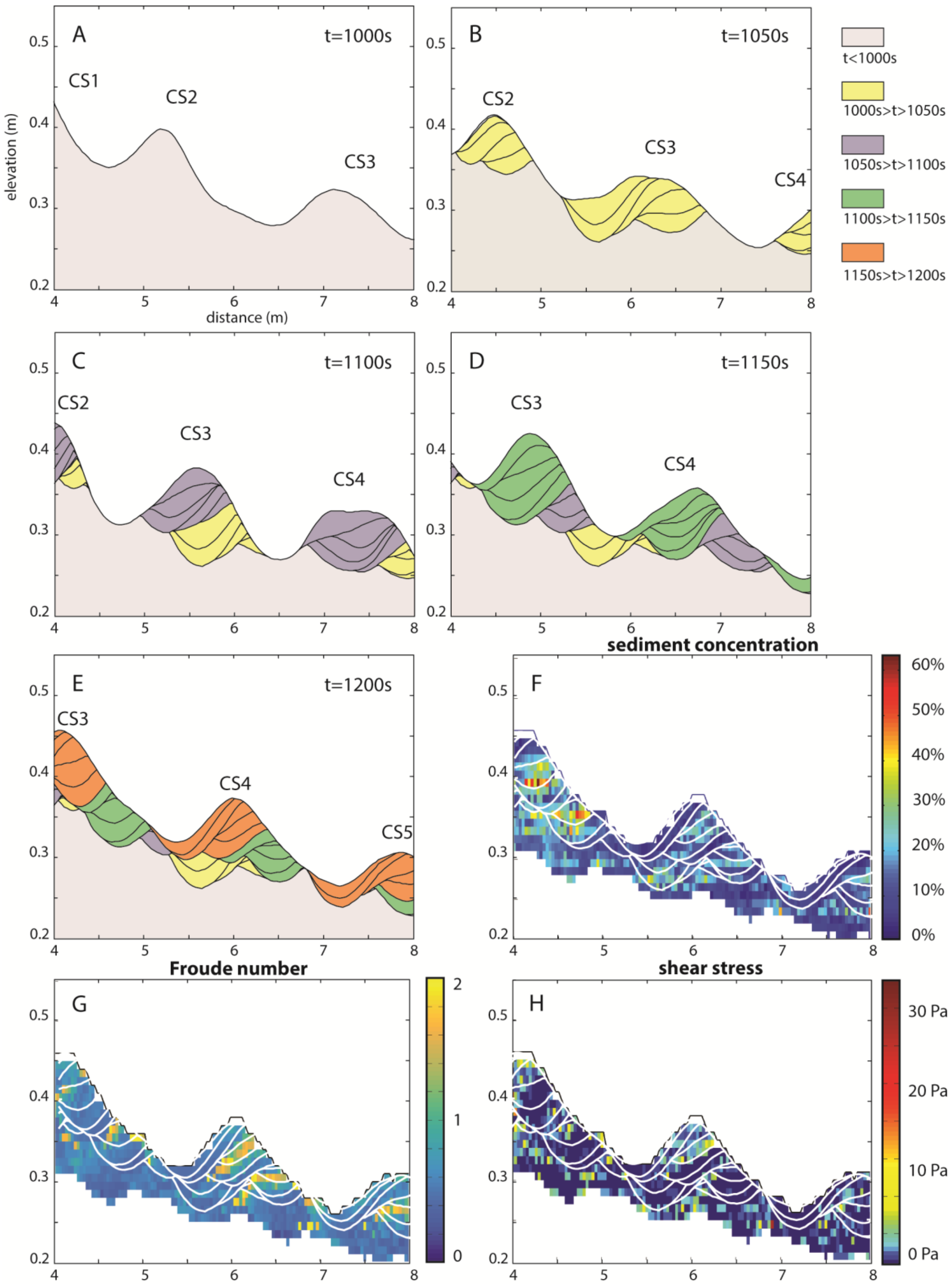
A
t=1000s
CS1
CS2
CS3
elevation (m)
distance (m)
B
t=1050s
CS2
CS3
CS4
t<1000s
1000s>t>1050s
1050s>t>1100s
1100s>t>1150s
1150s>t>1200s
C
t=1100s
CS2
CS3
CS4
D
t=1150s
CS3
CS4
E
t=1200s
CS3
CS4
CS5
sediment concentration
F
60%
50%
40%
30%
20%
10%
0%
Froude number
G
shear stress
H
30 Pa
20 Pa
10 Pa
0 Pa

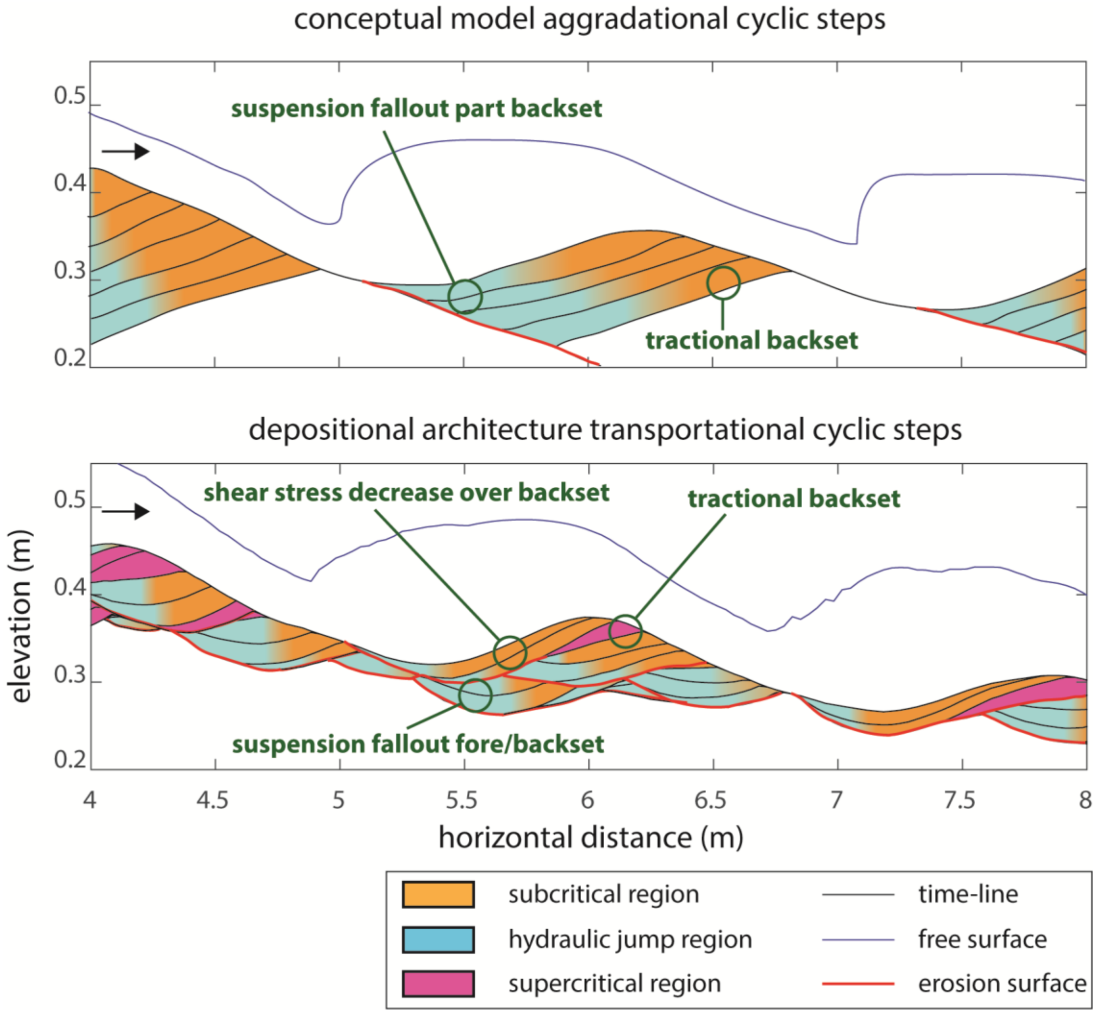
conceptual model aggradational cyclic steps
suspension fallout part backset
tractional backset
0.5
0.4
0.3
0.2
depositional architecture transportational cyclic steps
shear stress decrease over backset
tractional backset
suspension fallout fore/backset
elevation (m)
4
4.5
5
5.5
6
6.5
7
7.5
8
horizontal distance (m)
subcritical region
hydraulic jump region
supercritical region
time-line
free surface
erosion surface